Journal of The Electrochemical Society, **150** (3) A385-A397 (2003)
0013-4651/2003/150(3)/A385/13/$7.00 © The Electrochemical Society, Inc.

Conduction in Multiphase Particulate/Fibrous Networks

Simulations and Experiments on Li-ion Anodes

C.-W. Wang,[a] K. A. Cook,[b] and A. M. Sastry[a,b,*,z]

[a]*Department of Mechanical Engineering and* [b]*Department of Biomedical Engineering, University of Michigan, Ann Arbor, Michigan 48109-2125 USA*

Several promising Li-ion battery technologies incorporate nanoarchitectured carbon networks, typically in the form of whisker/particle blends bonded with thermoplastic binders to form the anodes. Degradation of these materials is currently a persistent problem, with damage presenting as blistering and/or delamination of the electrode. Both material composition and morphology play a role in these critical failure modes, and are explored in the present work as they affect conduction in practical battery materials. Lawrence Berkeley National Laboratories and the Institut de Recherche d'Hydro-Quebec supplied the materials studied in this work. Our present approach builds on our previous numerical work, incorporating real material morphology and careful selection of boundary conditions to reduce the numerical difficulties posed by singularities in the field solution, due to phase contrast, sharp corners, etc. In order to allow use of these models for various shapes of particles, we provide a few simple geometrical relations for calculation of total surface area for various morphologies of electrode materials. A four-point-probe technique was employed to obtain the experimental conductivities. Although the existence of contact resistance is well known, there is little literature regarding a technique to measure its value; here, we also present a method for quantifying it, assuming that the anode layer is comprised of two layers. Voltage functions for each layer are determined by enforcement of voltage continuity at the interfaces, current intensities at the inlet and outlet on both sides of interface, and assumption of zero voltage in the second layer as $z \to \infty$. The four-point-probe technique is suitable for the electrode materials tested, offering reasonable experimental precision in a simple setup. The results of this study offer some insight into the design of active materials. The model shows applicability to a wide variety of materials, including those comprised of fibers, particles, and flakes. Comparisons among simulation predictions and real material conductivities showed very good agreement. An obvious subject of future work is combined electrochemical, conduction, and mechanical modeling of these materials.
 [DOI: 10.1149/1.1543566]

Manuscript submitted January 28, 2002; revised manuscript received August 31, 2002. Available electronically February 7, 2003.

Several promising Li-ion battery technologies incorporate nanoarchitectured carbon networks, typically in the form of whisker/particle blends bonded with thermoplastic binders to form the anodes. Degradation of these materials is currently a persistent problem, with damage presenting as blistering and/or delamination of the electrode.

Various carbon additives have been used in anodes to reduce failures and improve performance. In the present work, we are interested primarily in electrical conduction in the electrodes. Because performance variability is related to material variability, we generate a large number of ''realizations'' in our computational modeling, to simulate the variance that real materials have. We validate our computational models with measured resistivities of experimental anode materials, and also present descriptions of novel data analysis techniques required for the validation.

Conduction and performance of Li-ion anode materials.—Multiaxial loads are induced in electrodes during electrochemical cycling, causing morphology changes which not only alter the mechanics of load transfer within the materials, but also reduce interparticle contact, and thus conductivity. Electrical conductivity is a key factor in cell performance; cell power is a linear function of the open circuit voltage V_{oc}, and the internal resistance R_b, as

$$P = IV = I(V_{oc} - IR_b) \quad [1]$$

The internal resistance is the aggregate of the electrolyte resistance R_s, the interface resistance between the electrolyte and electrodes R_{in}, the resistance between the current collectors and electrodes R_c, and the electrode materials resistance, R_e[1] Using A and C to represent anode and cathode, respectively, this internal resistance can be expressed[1] as

$$R_b = R_s + R_{in}(A) + R_{in}(C) + R_c(A) + R_c(C) + R_e(A) + R_e(C). \quad [2]$$

wherein resistance between the electrolyte and electrode is proportional to the ratio of the actual surface area of the electrode to the nominal (flat) interface area.

High energy density materials for Li-ion secondary batteries have several deficiencies in practical application. For example, lithium metal, desirable in anodes because of its high energy density (3862 mAh g^{-1}, per Table I) is highly reactive with organic electrolyte solvents. This reactivity results in a nonuniform passivation, or film formation on the anode surface. Furthermore, dendrite growth on lithium metal can cause short circuits in cells.

Carbons have been studied as anodes in Li-ion cells with lithiated metal oxides, *e.g.*, $LiCoO_2$, $LiNiO_2$, and $LiMn_2O_4$ as cathode materials. Herold[2] first reported the chemical intercalation of Li ions into graphite; commercial graphite intercalation compounds (GICs) have been greatly refined since that time. Because they are less reactive than lithium metal, stable reversibility can be achieved, with a theoretical potential that is only 0.5 eV less than that of lithium metal.

The capacities and electrochemical performances of graphitized carbon materials depend on the distance between basal planes d_{002}, surface area, and the electrolyte systems used. Table I gives several structural parameters and capacities for graphitized carbon materials, including natural graphite, mesocarbon microbeads (MCMBs),[3,4] and mesophase-pitch-based carbon fibers (MPCFs).[5] The theoretical limiting capacity of graphitized carbon anodes, 372 mAh g^{-1}, is somewhat less than that provided by hard carbons (500 mAh g^{-1}) as shown by Buiel *et al.*,[6] though hard carbons have shown a larger irreversible capacity (150 mAh g^{-1}) compared with that (30 mAh g^{-1}) of MCMBs. The graphitic materials are prone, however, to formation of ternary graphite intercalation compounds [e.g., $Li(solv)_y C_n$] resulting in swelling of the graphitic matrix. This swelling usually leads to a deterioration or exfoliation of the graphite matrix and a dramatic decrease in available capacity.

Electrode resistivity is a function of resistivity of active materials, contact resistance, and resistivity of current collector. Improved

* Electrochemical Society Active Member.
z E-mail: amsastry@umich.edu

Table I. Structural parameters and electrochemical performance of graphitized natural graphite, MCMB, and mesophase carbon fiber (MPCF).

Materials	Interlayer spacing d_{002} (Å)	Crystalline size L_c (Å)	Capacity (mAh/g)
Natural graphite	3.34	-	330
MCMB[3-4]	3.37	460	282
MPCF[5]	3.36	170	286
Hard carbon[6]	-	-	520
Lithium metal	-	-	3862

anode performance via addition of conductive carbons in Li-ion secondary batteries has been demonstrated in various Li-ion electrochemistries[3-15] through interruption of solvent cointercalation into basal planes. Solvent cointercalation is governed by the texture of the GICs, which varies with material type (natural graphite, mesocarbon microbeads, carbon fibers, etc.) Several workers[3,4,7] have attempted to reduce electrolyte decomposition on graphite via combination of material types on the anode, *e.g.*, mixing of flaky and spherical graphite.[7] Addition of conductive carbons in Li-ion secondary batteries has also been explored.[8-13] Larger, metallic fibers (with lengths and diameters on the order of micrometers) were shown by Ahn[8] to improve anodic conductivity, capacity, and high rate capability. Takami *et al.*[9] and Osaki *et al.*[10] showed that the MPCFs used as anodic materials for lithium-ion cells offered higher capacity rates and greater reversibility than those of graphitic anode materials. Endo *et al.*[11] characterized the nanostructure of MPCFs through Raman spectroscopy, and linked specific structural features tailored by different heat-treatment history of milled mesophase-pitch-based to improved performance. They also showed B-doped milled mesophase-pitch-based carbon fibers to have enhanced specific capacities and columbic efficiencies relative to undoped milled mesophase-pitch-based carbon fibers. More recently, chopped vapor grown carbon fibers (VGCFs) have been studied in detail as a conductive additives to Li-ion anodes. Endo *et al.*[12] linked the structural features of these fibers to improved cell performance. Others, including Tatsumi *et al.*[13] have compared various manufacturing techniques for the materials, showing, for example, that VGCFs produced by chopping after graphitization provide higher capacity than those produced by chopping before graphitization. Improvements in cell performance with carbon materials has been shown by several researchers, including Suzuki *et al.*[14] and in cylindrical configurations by Abe *et al.*,[15] though there is evidence that high aspect ratio (length/diameter) fibers pose a risk in cells due to the potential for puncture of separator material, leading to shorts.[16] MCMBs have also been shown to be good candidates for lithium-ion intercalation. Various treatments of the MCMB materials have been described, including those by Mabuchi *et al.*[3,4] who examined the effects of different heat-treatments on lithium-ion intercalation, finding that higher temperatures in the range examined (2000-2800°C) improved capacity.

Recent work thus suggests that conductive carbons as additives, made by a variety of manufacturing techniques (including graphitizable and nongraphitizable carbons, commingled with binders such as poly(vinylidene fluoride), PVdF) are advantageous in secondary batteries. Here, we focus on numerical modeling and experimentation on specific features in Li-ion anodes of such conductive elements. Anodic materials in common use for improved conduction, capacity, and high rate capability include metallic and carbon particles, fibers, and whiskers. These materials range in size and shape from the microscale to the nanoscale. We focus our efforts on simulations of conduction in disordered structures spanning these shapes and sizes. Though other electrochemical phenomena (*e.g.*, solvent cointercalation) are undoubtedly important in conduction, we focus on the conduction of the particles alone, especially on particle selection and ultimately, expansion of these models to encompass electrochemical reaction.

Materials studied, and key relations.—Lawrence Berkeley National Laboratories (LBNL) and the Institut de Recherche d'Hydro-Québec (IREQ) supplied the materials studied in this work. Compositions of the materials and manufacturing methods are listed in Table II. We performed image analysis of material composition via atomic force and scanning electron microscopy (SEM) to determine particle shapes and distributions in the as-manufactured electrodes. Examples of these images are shown for materials 1 and 3 in Fig 1b, c, and d. Anodes designated as ''laminated'' were compressed by the suppliers during the manufacturing process to reduce thickness.

Conduction modeling: porous, heterogeneous materials.—There is a large body of literature on determining effective material properties, including conductivity of porous and/or inhomogeneous materials. Classical theories proposed by Maxwell-Garnett,[17] Bruggeman,[18] and Meredith and Tobias,[19] have formed the underpinnings of more recent efforts, which similarly base prediction of conductivity on volume fractions and material properties of conductive materials. These models assumed an ''effective'' composition with particles of smooth or regular shape (*e.g.*, circular inclusions first analyzed by Maxwell-Garnett[17]) embedded in other more- or less-conductive phases. Green's function formulations have also been employed (*e.g.*, Ref. 20) to solve for conduction in media containing inclusions of greater complexity; for example, a Green's function derivation of electric field for ellipsoidal inclusion was more recently given by Choy.[21] Other closed-form solutions, influenced by those originally provided by Hashin and Strikman,[22] have used variational principles to obtain conductivity of heterogeneous materials.

Previous numerical work in percolation in identifying critical volume fractions for effective conduction in materials (*e.g.*, those by Kirkpatrick[23] and Pike and Seager[24]) has shown that the percolation probability, defined as the probability of being connected to an infinite cluster, has a finite percolation threshold concentration dependent on shape of conductive inclusions and/or particles. Kirkpatrick showed conductivity, σ, to be proportional to the power law of the difference of percolation probability, p, p_c, and percolation threshold, as

Table II. Material compositions and processing conditions of the anode materials from Lawrence Berkeley National Laboratories and the Institute de Recherché d'Hydro-Quebec.

Material	Source	Composition: Natural graphite (v.f. %)	Composition: MCMB (v.f. %)	Composition: Carbon fiber (v.f. %)	Composition: PVdF (v.f. %)	Processing condition
Material 1	LBNL	23.36	-	-	4.11	Nonlaminated
Material 2	LBNL	27.14	-	-	4.77	Laminated
Material 3	IREQ	-	21.50	4.89	6.34	Nonlaminated
Material 4	IREQ	-	22.30	6.60	5.10	Laminated
Material 5	IREQ	-	-	33.09	5.81	Nonlaminated
Material 6	IREQ	-	-	32.83	5.77	Laminated

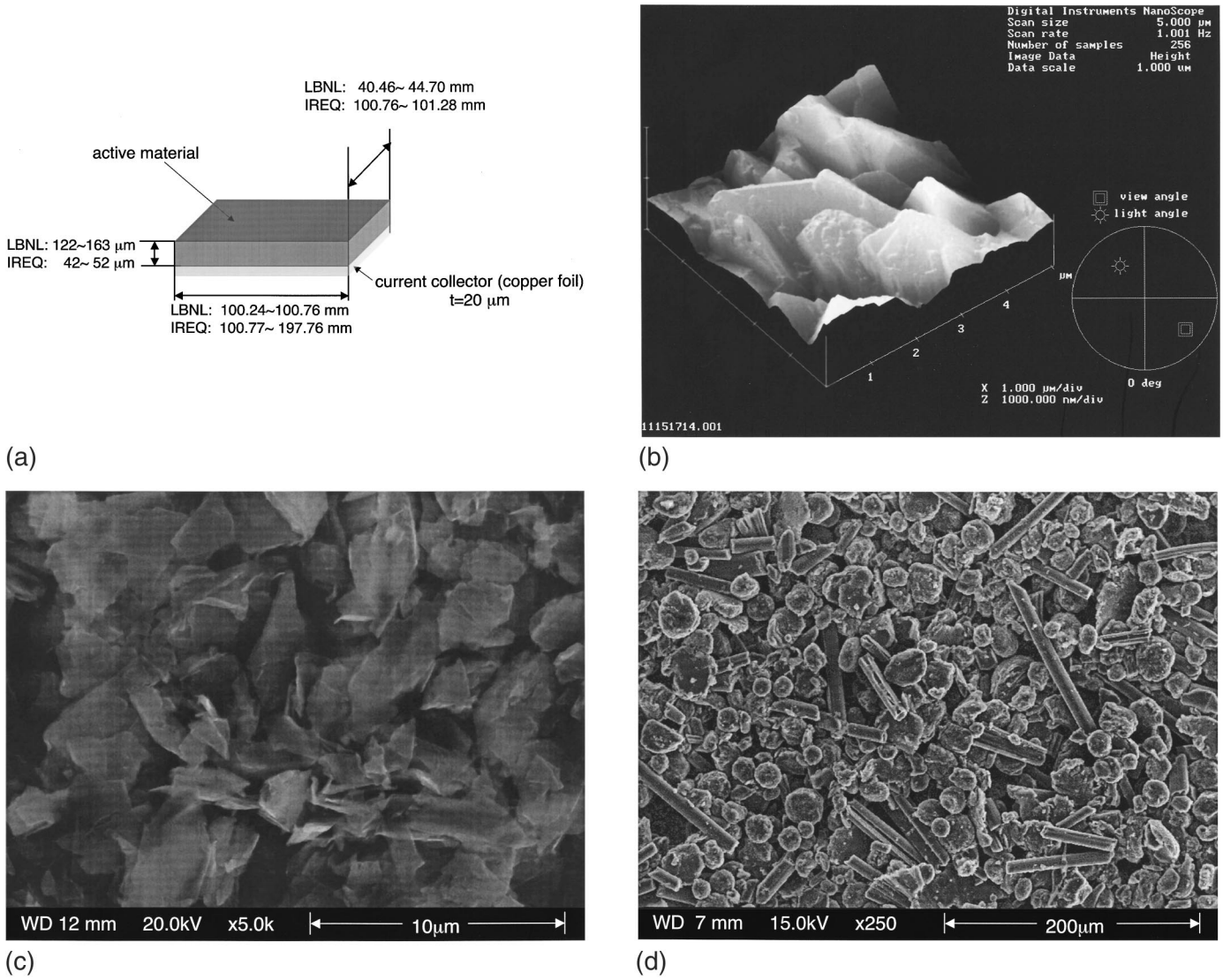

Figure 1. (a) The bilayer Li-ion battery anode. The top layer is an active material comprised of graphitized carbon material and polymer binder; the lower layer is a current collector, comprised of a copper foil. An atomic force microscope image of the natural graphite of the anode active material is shown for reference in (b); a scanning electron micrograph (SEM) of the same material is shown in (c). (d) An SEM image of material 3.

$$\sigma(p) \propto (p - p_c)^t \qquad [3]$$

Our own previous numerical work has also shown quantitatively that moderate increases in particle aspect ratio (AR) for low density materials provide significant improvements in electrical conductivity,[25] since the percolation point was reduced dramatically.[26] Indeed, we have recently presented closed-form solutions to the (two-dimensional) 2D[27] and 3D[28] percolation problems for generalized ellipses and ellipsoids, respectively, verifying our earlier results and expanding them to allow calculation of percolation, theoretically, in multiphase arrays as well.

However, the mechanical stresses in such heterogeneous systems depend heavily on particle and interconnect geometry,[29-32] and thus require direct simulation in solution. Because of the need to simulate both the mechanics and conductivity of these materials, our present approach builds on our previous numerical work, incorporating real material morphology and careful selection of boundary conditions to mitigate the numerical difficulties posed by singularities in the field solution. Figure 2 shows examples of the approach, with effective conductivities calculated for arrays of particles.

Experimental

The Li-ion anode is a bilayered structure, comprised of graphitic active material of relatively low conductivity deposited on a current collector comprised of a highly conductive copper alloy. The thin, multilayered anodes studied here have some physical similarity to semiconductor wafers, wherein conductivity differences between layers arise from impurities. In order to experimentally determine the conductivity of each layer of the anode, several methods were examined, described briefly as follows.

Eddy current technique.—In this approach, resistivity is determined without contact between probe and specimen. An eddy current is induced in the specimen by an oscillating magnetic field. Although the lack of contact makes this approach entirely nondestructive, it is highly sensitive to surface defects, including the cracks common in anode materials.

Two-point-probe technique.—This approach utilizes two probes, which simultaneously deliver current and measure voltage on the surface of the specimen. Hence, the contact and spreading resistances at the interfaces of probes and specimen must be estimated to

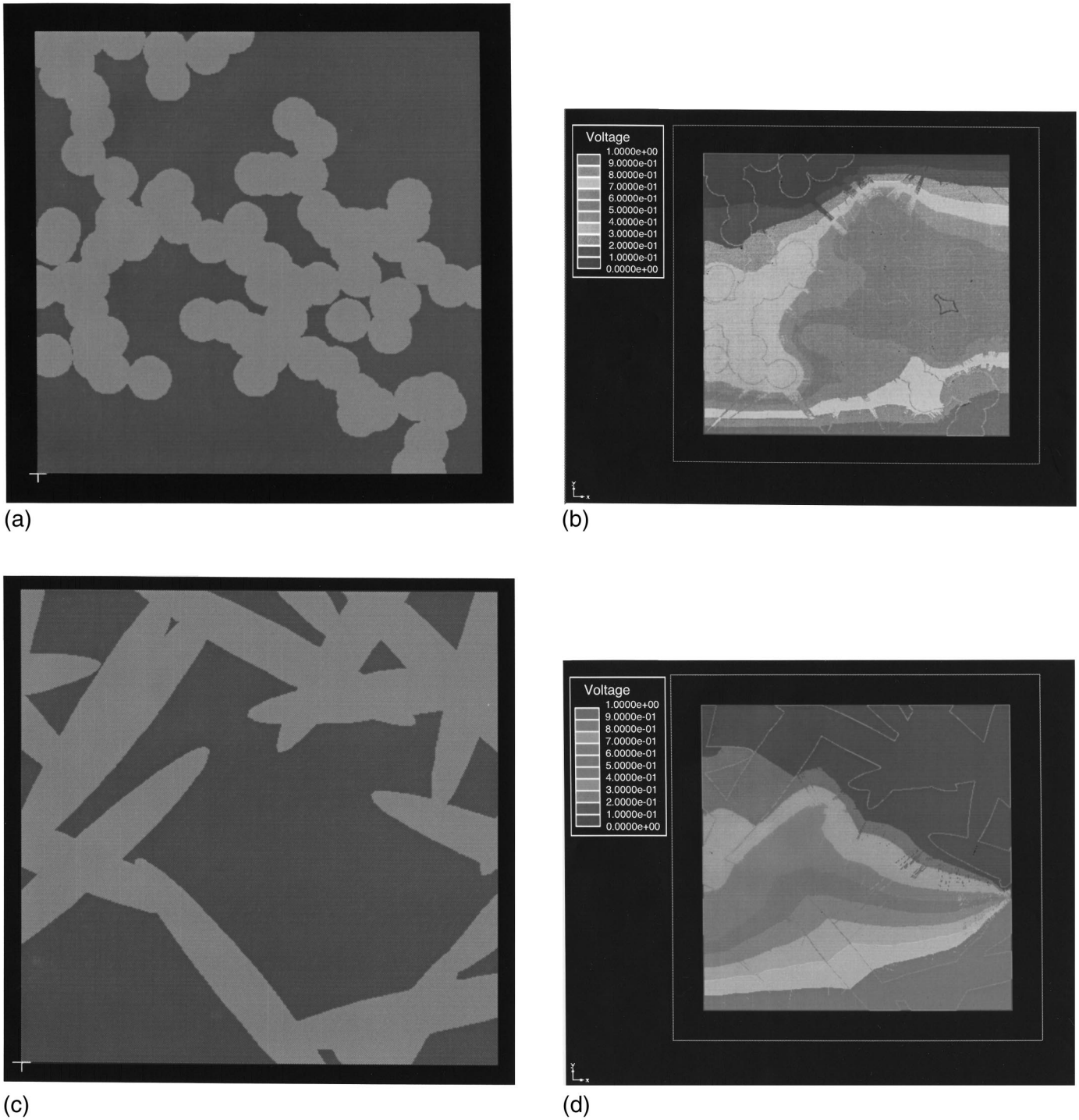

Figure 2. Networks and voltage distributions in simulated domains, with reduced volume fraction of 42%, (a,b) comprised of particles with aspect ratio 1, and (c,d) ellipses with fixed length and fixed ratio of major axis to minor axis of 7. Boundary conditions prescribed for simulations are 1.0 V at the bottom edge and 0.0 V at the top edge; all particles were assumed to have conductivity of 1.

interpret experimental resistivity. Correction factors for analysis of finite volumes and various boundary conditions using the approach were given by Dicky,[33] and a detailed comparison of the approach with the four-probe experiment was provided by Albers *et al.*[34]

Four-point-probe technique.—Various geometrical configurations of four surface probes (collinear in-line, symmetrical circular, or square geometry) are placed on the specimen surface to measure resistivity. Current is channeled through two probes; voltage across the other two probes is measured. Layerwise resistivities in a multilayered specimen are determined by indirect calculation, incorporating specimen geometry, probe position, probe spacing, and geometrical correction factors. Because contact and spreading resistances (Eq. 2) are not directly measured at the voltage-measuring inner probes, the four-probe experiment is widely viewed as more accurate than the two-probe technique (e.g., Ref. 35).

Approach: theoretical underpinnings and analysis.—Here, the four-point-probe technique was used as shown in Fig. 3a, with current input and output between the two outer probes, and voltage

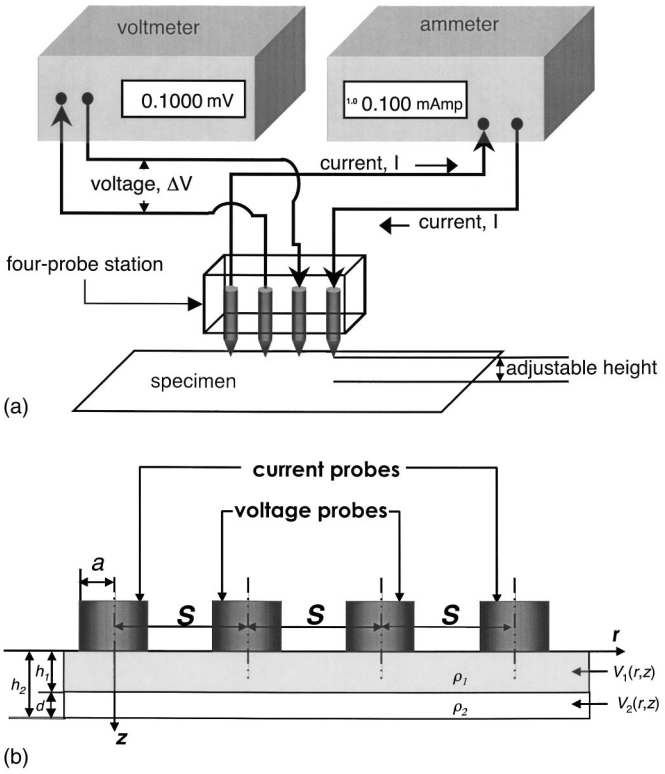

Figure 3. (a) Schematic of test apparatus (four-point-probe) used in the measurement of resistivity. (b) In the four-probe experiment, current is cycled through the first and fourth probes; voltage difference is measured between the second and the third inner probes.

difference measured between the two inner two probes (Fig. 3b). Analysis of the experiment to determine both top layer and contact resistivity required extension of a classic approach, described presently.

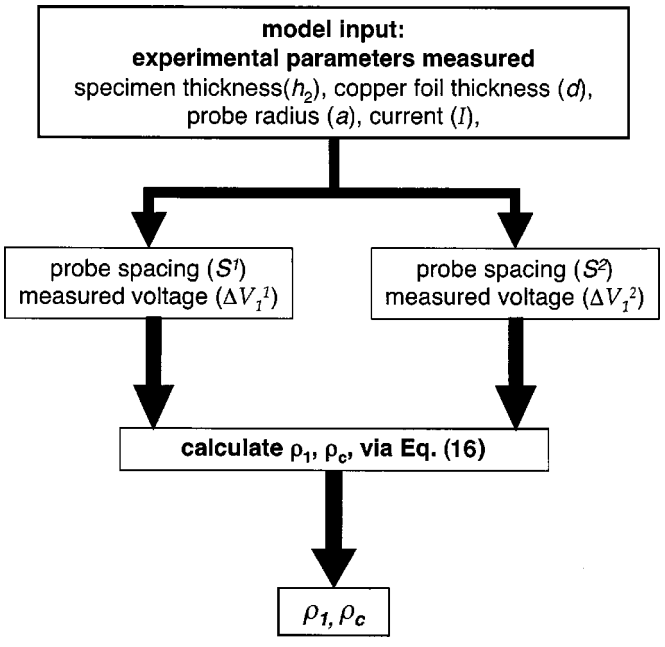

Figure 4. Flow chart for data analysis for the four-probe experiment. ΔV_1^1 and ΔV_1^2 are two measured voltage readings corresponding to S^1 and S^2 for two different probe spacings.

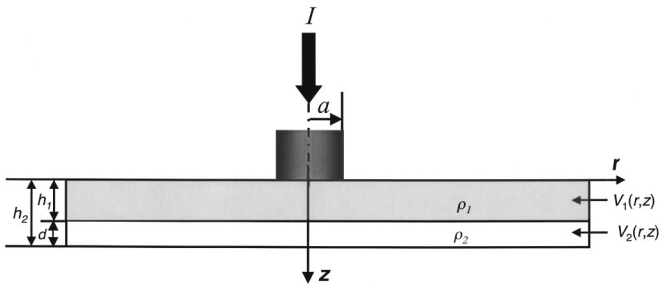

Figure 5. In the single probe, current is delivered to an infinite two-layer medium.

Two methods are commonly employed to interpret experimental data for the four-probe experiment. One method is the "image approach" which assumes that the top layer has a uniform resistivity and that the substrate layer is either perfectly conducting or perfectly insulating (*e.g.*, early work by Valdes[36]); this approach is not appropriate for multilayered structures. Another common interpretive technique for the four-point-probe method is the Schumann-Gardner multilayer theory.[37] In this approach, which we extended here, diffused resistivity profiles for each N layers are approximated by assuming that Laplace's equation is the valid governing equation, and that there is no electron accumulation in the materials (*i.e.*, no self-capacitance). These assumptions have been amply verified in the literature (*e.g.*, Ref. 37-39). However, the Schumann-Gardner approach does not explicitly provide an estimate for contact resistance. Because imperfect contact between the graphitized carbon anodic material and the copper foil current collector can result in contact resistance, we solve for both for top-layer (active material) resistivity and contact resistance per the technique shown in Fig. 4.

Delivery of input current through the probes induces voltage distributions inside the specimen. To determine the top layer and contact resistivities, the distributions of voltage must be determined. Application of boundary conditions allows for solution of the voltage functions in terms of specimen thicknesses, resistivities, and probe spacing. The resistivities are then determined using experimental data, *i.e.*, measured voltage drops and known current input.

Voltage is a scalar variable. Therefore, the voltage distribution between the second and third probes can be evaluated by superposition. We first discuss the voltage distribution induced by one probe, then superimpose the voltage distributions due to two current input/output probes, corresponding to the inline four-point-probe setup.

Single probe.—Laplace's equation is the governing equation for the voltage distribution in a semi-infinite medium totaling N layers, at each nth layer

$$\frac{\partial^2 V_n}{\partial r^2} + \frac{1}{r}\frac{\partial V_n}{\partial r} + \frac{\partial^2 V_n}{\partial z^2} = 0 \qquad [4]$$

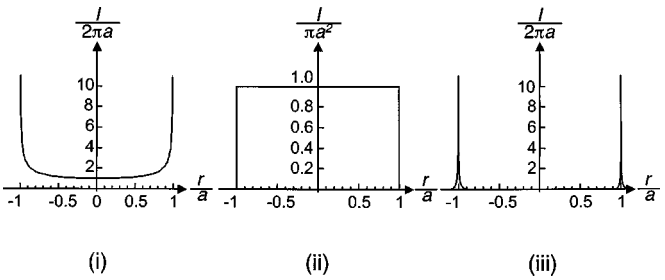

Figure 6. The current distributions profile due to (*i*) equipotential as in Eq. 6, (*ii*) uniform current intensity as in Eq. 7, and (*iii*) Dirac delta as in Eq. 8.

In Eq. 4, the voltage function for the nth layer can be expressed as

$$V_n(r,z) = \int_0^\infty \theta_n(\lambda) J_0(\lambda r) e^{-\lambda z} d\lambda + \int_0^\infty \psi_n(\lambda) J_0(\lambda r) e^{\lambda z} d\lambda \quad [5]$$

where λ is the integration variable. For probes of radius a as shown in Fig. 3b, the kernel functions θ_n and ψ_n depend on the specimen layer thicknesses, material properties and current distribution.

In order to find the particular solution to Eq. 5 for one probe (Fig. 5) where a constant current I flows through the surface layer, $2n$ boundary conditions are required, because the voltage function V_n of each layer has two unknowns, θ_n and ψ_n. The anode as shown in Fig. 5, comprises of two layers, with resistivities ρ_1 and ρ_2, and voltage functions, V_1 and V_2, respectively. To determine functions V_1 and V_2 explicitly, four boundary conditions are needed:

1. A functional form for I, the total current flowing into a flat circular area of radius a, on an infinite domain, must be made. There are several possible assumptions for this function, including a distribution due to an equipotential underneath the probe

$$-\frac{1}{\rho_1}\frac{\partial V_1(r,z)}{\partial z} = \begin{cases} \dfrac{I}{2\pi a\sqrt{a^2 - r^2}} & \text{if } |r| \leq a \text{ and } z = 0 \\ 0 & \text{if } |r| > a \text{ and } z = 0 \end{cases} \quad [6]$$

a uniform current distribution

$$-\frac{1}{\rho_1}\frac{\partial V_1(r,z)}{\partial z} = \begin{cases} \dfrac{I}{\pi a^2} & \text{if } |r| \leq a \text{ and } z = 0 \\ 0 & \text{if } |r| > a \text{ and } z = 0 \end{cases} \quad [7]$$

or Dirac delta distribution

$$-\frac{1}{\rho_1}\frac{\partial V_1(r,z)}{\partial z} = \frac{I}{2\pi r}\delta(r - a) \quad [8]$$

Each of these is shown schematically in Fig. 6. One may also assume any linear combination of these three assumptions. Here, we assumed the current density to be normally distributed as in Eq. 6, because this assumption produces less oscillatory behavior in the voltage functions than the other two functions. Detailed descriptions of the various assumed current distributions were discussed by Berkowitz and Lux,[40] who found little effect (less than 10%) on calculated resistivity for these distributions.

2. At the first interface, $z = h_1$, the current density is the same across the boundary, as

$$\frac{1}{\rho_1}\frac{\partial V_1(z,r)}{\partial z}\bigg|_{z=h_1} = \frac{1}{\rho_2}\frac{\partial V_2(z,r)}{\partial z}\bigg|_{z=h_1} \quad [9]$$

3. For the more general case, where the contact resistance is taken into account, the potential difference between the first layer and the second layer can be calculated by multiplying the current density, j, and the contact resistacne, ρ_c

$$V_1(z,r)|_{z=h_1} - V_2(z,r)|_{z=h_1} = -j\rho_c \quad [10]$$

4. There is no current flowing out of the bottom of the second layer at $z = h_2$

$$\frac{\partial V_2(z,r)}{\partial z}\bigg|_{z=h_2} = 0 \quad [11]$$

Applying these boundary conditions, we find for a single probe

$$V_1(r,z) = \frac{I\rho_1}{2\pi a}\int_0^\infty \frac{\begin{bmatrix} -e^{z\lambda-2h_2\lambda}(\rho_1+\rho_2-\lambda\rho_c) + e^{-2d\lambda-z\lambda}(\rho_1-\rho_2+\lambda\rho_c) \\ +e^{z\lambda-2h_1\lambda}(\rho_1-\rho_2-\lambda\rho_c) - e^{-z\lambda}(\rho_1+\rho_2+\lambda\rho_c) \end{bmatrix}}{\lambda\begin{bmatrix} e^{-2h_2\lambda}(\rho_1+\rho_2-\lambda\rho_c) + e^{-2d\lambda}(\rho_1-\rho_2+\lambda\rho_c) \\ -e^{-2h_1\lambda}(\rho_1-\rho_2-\lambda\rho_c) - (\rho_1+\rho_2+\lambda\rho_c) \end{bmatrix}}[J_0(\lambda r)]\sin(\lambda a)d\lambda \quad [12]$$

$$V_2(r,z) = \frac{I\rho_1}{2\pi a}\int_0^\infty \frac{-2\rho_2(e^{-z\lambda} + e^{-2h_2\lambda+z\lambda})}{\lambda\begin{bmatrix} e^{-2h_2\lambda}(\rho_1+\rho_2-\lambda\rho_c) + e^{-2d\lambda}(\rho_1-\rho_2+\lambda\rho_c) \\ -e^{-2h_1\lambda}(\rho_1-\rho_2-\lambda\rho_c) - (\rho_1+\rho_2+\lambda\rho_c) \end{bmatrix}}[J_0(\lambda r)]\sin(\lambda a)d\lambda$$

Four Probes.—Using superposition, the voltage functions between the inner two probes for a two-layered specimen, for an inline four-point-probe seen in Fig. 3b, can be expressed as

$$\Delta V_1(S,z) = 2[V_1(S,z) - V_1(2S,z)]$$
$$\Delta V_2(S,z) = 2[V_2(S,z) - V_2(2S,z)] \quad [13]$$

The bracketed expressions in Eq. 13 are multiplied by a factor of 2 because the fourth probe draws out the current, which has the same effect as delivering current to the first probe. Substitution of Eq. 12 into Eq. 13, we find for the voltage functions between the second and third probe (for each layer 1 and 2)

$$\Delta V_1(S,z) = \frac{I\rho_1}{\pi a}\int_0^\infty \frac{\begin{bmatrix} -e^{z\lambda-2h_2\lambda}(\rho_1+\rho_2-\lambda\rho_c) + e^{-2d\lambda-z\lambda}(\rho_1-\rho_2+\lambda\rho_c) \\ +e^{z\lambda-2h_1\lambda}(\rho_1-\rho_2-\lambda\rho_c) - e^{-z\lambda}(\rho_1+\rho_2+\lambda\rho_c) \end{bmatrix}}{\lambda\begin{bmatrix} e^{-2h_2\lambda}(\rho_1+\rho_2-\lambda\rho_c) + e^{-2d\lambda}(\rho_1-\rho_2+\lambda\rho_c) \\ -e^{-2h_1\lambda}(\rho_1-\rho_2-\lambda\rho_c) - (\rho_1+\rho_2+\lambda\rho_c) \end{bmatrix}}[J_0(S\lambda) - J_0(2S\lambda)]\sin(\lambda a)d\lambda \quad [14]$$

$$\Delta V_2(S,z) = \frac{I\rho_1}{\pi a}\int_0^\infty \frac{-2\rho_2(e^{-z\lambda} + e^{-2h_2\lambda+z\lambda})}{\lambda\begin{bmatrix} e^{-2h_2\lambda}(\rho_1+\rho_2-\lambda\rho_c) + e^{-2d\lambda}(\rho_1-\rho_2+\lambda\rho_c) \\ -e^{-2h_1\lambda}(\rho_1-\rho_2-\lambda\rho_c) - (\rho_1+\rho_2+\lambda\rho_c) \end{bmatrix}}[J_0(S\lambda) - J_0(2S\lambda)]\sin(\lambda a)d\lambda$$

Table III. Overall resistance and contact resistivities for materials tested in this research.

Materials	Composition: Natural graphite (%)	Composition: Carbon fiber (%)	Composition: MCMB (%)	Composition: PVdF (%)	Carbon compound resistivity $\rho_1(\mu\Omega$ cm): Average	Carbon compound resistivity $\rho_1(\mu\Omega$ cm): Standard deviation	Contact resistivity $\rho_c(\mu\Omega$ cm^2): Average	Contact resistivity $\rho_c(\mu\Omega$ cm^2): Standard deviation	Uncertainty (w_{ρ_1}) (%)
Material 1	23.36	-	-	4.11	6.16×10^5	3.04×10^5	6.64×10^4	3.48×10^4	12.76
Material 2	27.14	-	-	4.77	1.63×10^5	5.74×10^4	2.11×10^4	7.25×10^3	16.90
Material 3	-	4.89	21.50	6.34	2.58×10^4	2.94×10^3	4.37×10^3	1.98×10^3	13.50
Material 4	-	6.60	22.30	5.10	2.40×10^4	2.85×10^3	3.96×10^3	1.41×10^3	17.53
Material 5	-	33.09	-	5.81	3.39×10^4	9.48×10^3	6.05×10^3	2.20×10^3	13.46
Material 6	-	32.83	-	5.77	5.39×10^4	3.55×10^4	9.59×10^3	6.75×10^3	17.58

When the contact resistance is neglected, these equations become identical to those derived by Schumann and Gardner,[37] as

$$\Delta V_1(S,z) = \frac{I\rho_1}{\pi a}\int_0^\infty \frac{\begin{bmatrix} -e^{z\lambda-2h_2\lambda}(\rho_1+\rho_2)+e^{-2d\lambda-z\lambda}(\rho_1-\rho_2) \\ +e^{z\lambda-2h_1\lambda}(\rho_1-\rho_2)-e^{-z\lambda}(\rho_1+\rho_2)\end{bmatrix}}{\lambda\begin{bmatrix} e^{-2h_2\lambda}(\rho_1+\rho_2)+e^{-2d\lambda}(\rho_1-\rho_2) \\ -e^{-2h_1\lambda}(\rho_1-\rho_2)-(\rho_1+\rho_2)\end{bmatrix}} \times [J_0(S\lambda)-J_0(2S\lambda)]\sin(\lambda a)d\lambda$$

$$\Delta V_2(S,z) = \frac{I\rho_1}{\pi a}\int_0^\infty \frac{-2\rho(e^{-z\lambda}+e^{-2h_2\lambda+z\lambda})}{\lambda\begin{bmatrix} e^{-2h_2\lambda}(\rho_1+\rho_2)+e^{-2d\lambda}(\rho_1-\rho_2) \\ -e^{-2h_1\lambda}(\rho_1-\rho_2)-(\rho_1+\rho_2)\end{bmatrix}} \times [J_0(S\lambda)-J_0(2S\lambda)]\sin(\lambda a)d\lambda \quad [15]$$

The measured voltage is related to input current on the surface of the top layer of the electrode ($z = 0$) as

$$\Delta V_1(S,z) = \frac{I\rho_1}{\pi a}\int_0^\infty \frac{\begin{bmatrix} -e^{-2h_2\lambda}(\rho_1+\rho_2-\lambda\rho_c)+e^{-2d\lambda}(\rho_1-\rho_2+\lambda\rho_c) \\ +e^{-2h_1\lambda}(\rho_1-\rho_2-\lambda\rho_c)-(\rho_1+\rho_2+\lambda\rho_c)\end{bmatrix}}{\lambda\begin{bmatrix} e^{-2h_2\lambda}(\rho_1+\rho_2-\lambda\rho_c)+e^{-2d\lambda}(\rho_1-\rho_2+\lambda\rho_c) \\ -e^{-2h_1\lambda}(\rho_1-\rho_2-\lambda\rho_c)-(\rho_1+\rho_2+\lambda\rho_c)\end{bmatrix}}[J_0(S\lambda)-J_0(2S\lambda)]\sin(\lambda a)d\lambda \quad [16]$$

Contact resistance and top-layer resistivity can be obtained inversely from Eq. 16 given the voltage difference between the second and the third probes, and the total current delivered. The resistivity of the second layer (copper foil for the anode) was assumed to be 1.71 $\mu\Omega$ cm.[41] In our experiments, we supplied the current and measured the experimental voltage; top layer resistivity, ρ_1, and the contact resistance, ρ_c were unknown. By varying probe spacing S, two paired values of $(S,\Delta V_1)$ were obtained, allowing determination of ρ_1 and ρ_c via substitution into Eq. 16 and solving the two expressions simultaneously.

Equation 16 comprises a challenging integral solution. Much effort was dedicated during the 1970s and 1980s, by workers including Choo *et al.*[39,42,43] in using various numerical methods, *e.g.*, Gauss-Laguerre quadrature and variational approaches, to solve such integrals containing both the Bessel function of the first kind and periodic functions. However, more recent advances in computational speed make these problems more tractable; so, in our work, we have solved the problem numerically.

The above derivations assumes that the substrate is a semi-infinite medium. Thus, it is important to place the probes sufficiently far from the specimen edge (*e.g.*, Ref. 35, wherein a distance between probes and edges of at least three times the probe spacing is recommended). Here, we maintained a probe placement of at least twelve times the probe spacing from the specimen edges. We note, however, that for probes which must be placed very close to the specimen edge, Eq. 16 can be rederived by assuming that another probe is placed on the nonconducting boundary, to correct for the edge effect.

Approach: methods and apparatus.—Specimens were placed on flat (insulating) plexiglas sheets, and a small input current was delivered through one outer probe and withdrawn from the other outer probe using a Digatron charge/discharge unit. An HP-34401A multimeter was used to measure the voltage difference between the second and third (inner) probes. This process was repeated for different probe spacings (1.4 and 2.8 mm), in the same approximate area on the anode surface, to obtain two different voltage readings. The conductivity of the top layer and contact resistance at that location were then obtained as described previously. Several sets of paired data were measured for the same specimen at different locations. Limitations suggested by Schroder[35] were generally followed, in which the ratio of sample width to probe spacing kept larger than 20, and the edge probes (probe 1 or 4) placed a distance at least three time larger than probe spacing from the specimen edge.

In order to determine the precision of our experimental technique, data uncertainties were also calculated. As seen in Eq. 16, the resistivity is function of probe radius a, probe spacing S, input current I, measured voltage difference V, the thickness of first layer h_1, and the thickness of the second layer h_2. Uncertainty can be calculated per Holman,[44] as

$$\frac{w_{\rho_1}}{\rho_1} = \sqrt{\left(\frac{\partial\rho_1}{\partial a}\frac{w_a}{\rho_1}\right)^2+\left(\frac{\partial\rho_1}{\partial S}\frac{w_s}{\rho_1}\right)^2+\left(\frac{\partial\rho_1}{\partial V}\frac{w_V}{\rho_1}\right)^2+\left(\frac{\partial\rho_1}{\partial I}\frac{w_I}{\rho_1}\right)^2+\left(\frac{\partial\rho_1}{\partial h_1}\frac{w_{h_1}}{\rho_1}\right)^2+\left(\frac{\partial\rho_1}{\partial h_2}\frac{w_{h_2}}{\rho_1}\right)^2} \quad [17]$$

where $w_{\rho 1}$ is the uncertainty in the result, and w_a, w_S, w_V, and w_{h2} are the uncertainties in the independent variables. Experimental results for materials 1 to 6 are shown in Table III.

Modeling Approach and Comparison with Data

Ansoft's Maxwell 2D finite element software was used, along with specialized codes to generate particle fields for analysis, to

Table IV. Assumed resistivities for constituents of materials tested.

	Resistivity ($\mu\Omega$ cm)
Natural graphite	6.00×10^3
MCMB	1.30×10^3
PVdF	1.00×10^{21}

determine conductivities of arrays of particles representative of the materials studied. Assumed resistivities of constituent materials are given in Table IV.[45-47] Our procedure for generating the microstructures modeled is illustrated in Fig. 7. First, statistical distributions of particle orientation, center point position, and aspect ratio (L/D) were obtained via image analysis, using National Institute of Health image analysis software[48] (Fig. 7a). Next, an initial network was generated numerically (Fig. 7b) using the statistical distributions found. Periodic boundary conditions were then enforced on the simulation array (Fig. 7c). Finally, extraneous (*i.e.*, nonconnected) particles were removed, based on the direction in which voltage was to be applied to the unit cell as shown (Fig. 7d). For each material analyzed, simulations were performed on twenty different realizations generated as described above. However, for material 2, the ARs of the constituent particles were small, resulting in only ten of the twenty models generated being percolated (*i.e.*, having non-negligible conductivity as a result of having at least one, continuous, domain-spanning conductive pathway). Details of these techniques were previously described by Cheng and Sastry.[26]

For material 1, percolated simulations in 2D model were not obtained, *i.e.*, model generation resulted in particle arrays which did not form continuous, domain spanning paths in the realizations, resulting in vanishingly small conductivities. Thus, for this material, no simulation results are presented. The Maxwell multiphase ap-

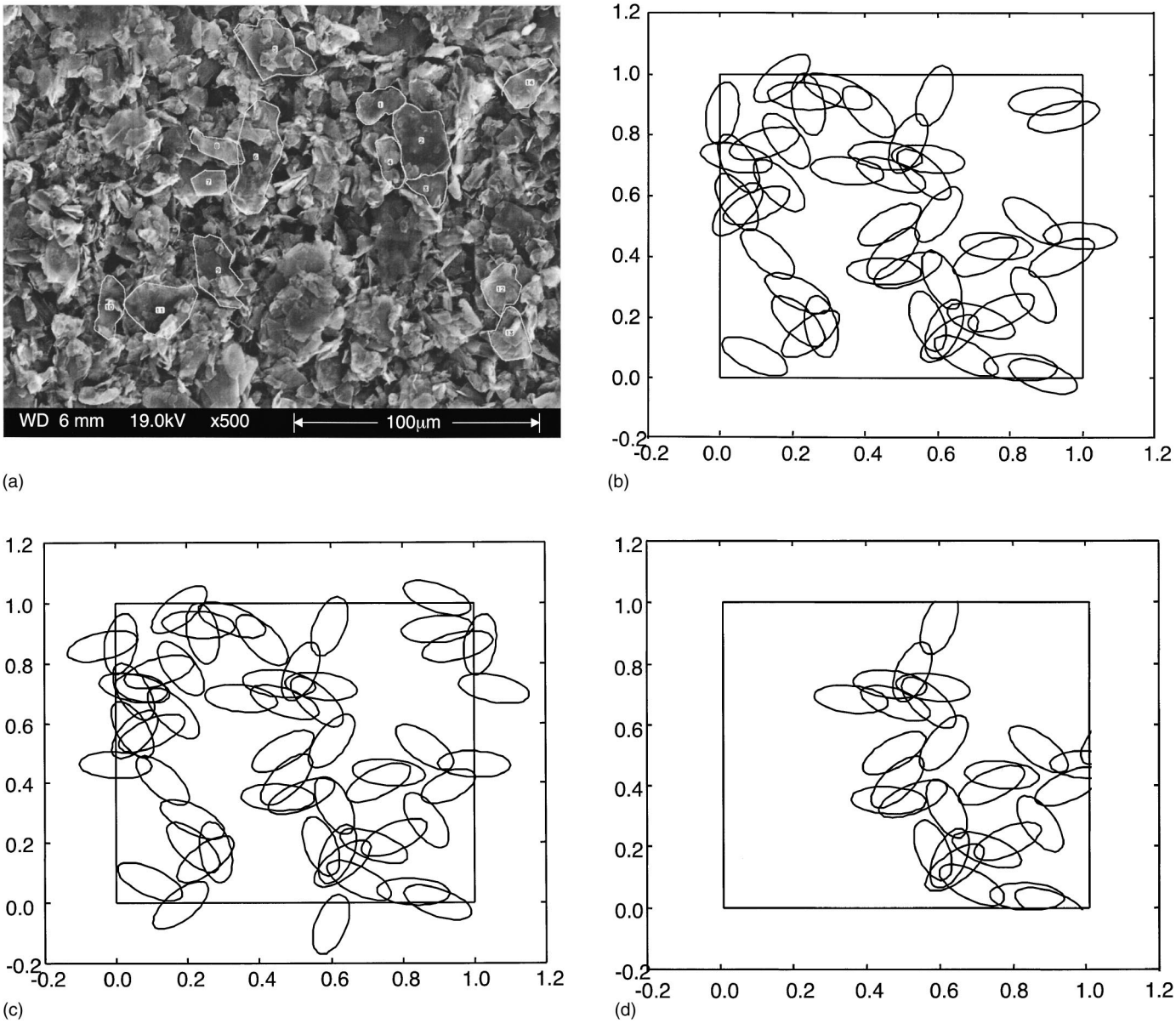

Figure 7. (a) Example of the procedure used in model generation for material 2, including analysis via NIH image software to measure particle orientation, shape and size from an SEM image, (b) generation of a numerical model of the cell with the same statistical distributions of orientations and shapes, and (c) enforcement of periodic boundary conditions on the array, preserving original specified volume fraction was maintained, (d) with removal of nonconducting particles from the unit cell.

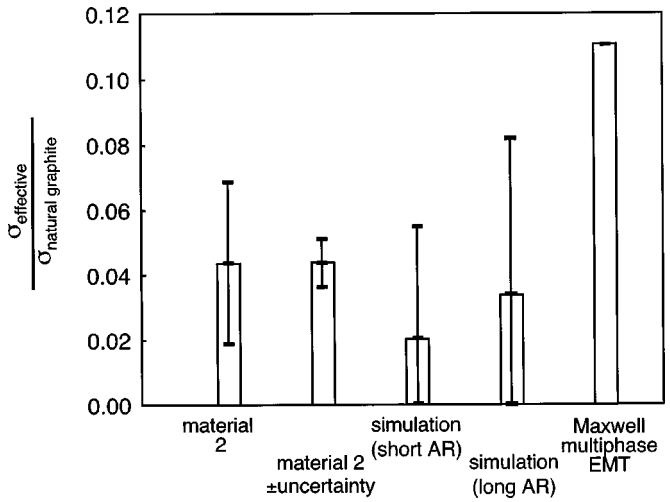

Figure 8. Simulation and experimental results for material 2 (LBNL), with the Maxwell multiphase effective medium theory for reference. Average ARs of 1.7 ± 0.41 were found; long AR describes simulations wherein ARs of 2.11 were used; short AR describes those in which ARs of 1.29 were used.

proach, which accounts only for the conductivities of the phases present in an averaged sense, predicts an overall normalized conductivity of 0.0922 for this material. The experimental results using the four-probe approach showed the material to have a normalized conductivity (carbon layer) of 0.0123, with standard deviation 0.0064. Thus, as for the other materials studied, the multiphase closed-form model significantly overestimated conductivity, though clearly our numerical approach incorrectly underestimated conductivity.

Figure 8 shows comparisons between simulation predictions and the normalized experimental results for conductivity ($\sigma_{\text{effective}}/\sigma_{\text{natural graphite}}$) for material 2. Image analysis showed that the particles' AR averaged 1.7, with a standard deviation of 0.41. Two types of numerical models were generated based on results of image analysis; long AR means that all particles had the same AR of 2.11, and short AR means that all particles had an AR of 1.29. Using these two extreme cases provided some bounds for comparison with real material data.

As shown in Fig. 8, the average conductivity predicted by the simulation is lower than that of the real material, and the variation is much larger, due to the low probability of percolation of the simulation models. Maxwell's classical multiphase result is shown for reference, where

$$\frac{K_m - 1}{2K_m + 1} = \sum_i \frac{(K_{d_i} - 1)f_i}{(2K_{d_i} + 1)} \qquad [18]$$

and each phase has volume fraction f_i and conductivity K_{di}, and K_m is the effective conductivity.

Figure 9a and b compare simulations and the normalized experimental results ($\sigma_{\text{effective}}/\sigma_{\text{MCMB}}$) for materials 3 and 4. Image analysis verified the spherical geometry, postprocessing, of the MCMBs (*i.e.*, ARs of 1), and showed ARs for carbon fiber averaging 6.8, with standard deviation of 6.8; fiber diameters were found to be 10 μm. In the numerical models, both particles and fibers were included. In Fig. 9a, simulations and experimental results are compared for material 3; simulation predictions bound the real material behavior, and the variation of conductivity of the material is close to the experimental uncertainty. As shown in Fig. 9b, similar results were obtained for material 4.

Figure 10a and b gives results for simulations and experiments on materials 5 and 6. Image analysis showed that the average AR of the carbon fibers was 6.8 with standard deviation 6.8 and the fiber diam was 10 μm. Two types of numerical models were generated

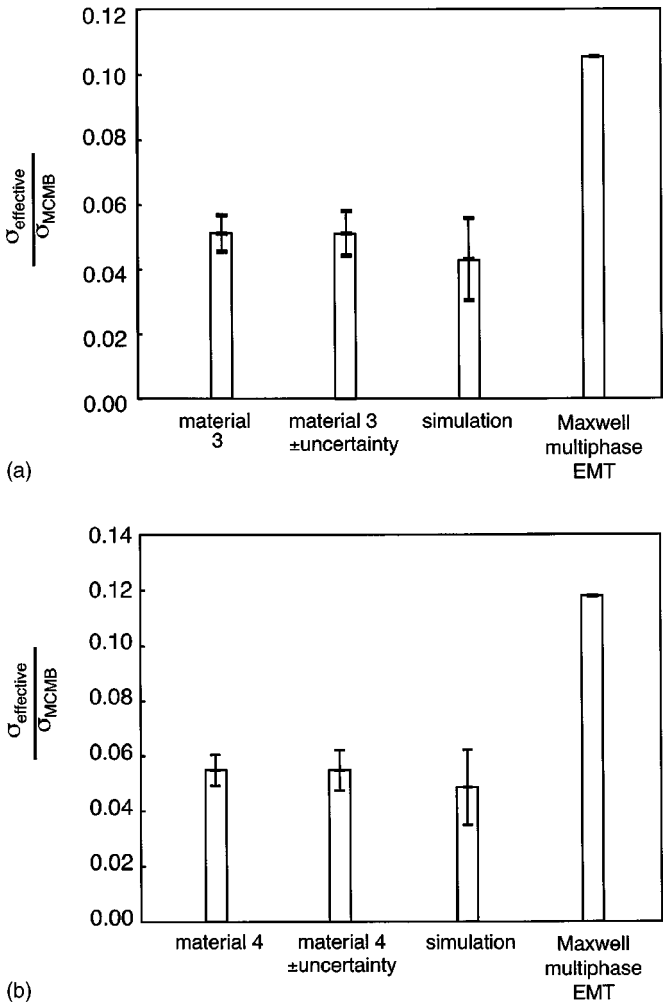

Figure 9. Simulation and experimental results for IREQ MCMB/fibrous nonlaminated (material 3) and laminated (material 4) materials are shown in (a) and (b), respectively. Simulation models assumed normally distributed fibers of average aspect ratio 6.8 ± 6.8, based on image analysis with circle particles. The Maxwell multiphase effective medium theory is given for reference.

for comparison, including "fiber only" realizations in which the volume fractions of PVdF were discarded, and "total volume" realizations which included the volume fraction of PVdF and carbon fibers. For each model, the ARs of the fibers were generated by normal distribution with an average of 6.8 and standard deviation of 6.8, based on image analysis results. Fiber only models were generated because SEM images showed the fibers to have very clean surfaces, as in Fig. 11. In simulating the total volume, we attempted to assess the importance of the PVdF binder in conduction. In Fig. 10a, we see that the prediction for conductivity of the "total" model is almost identical to the real material, and the prediction of the fiber only underestimates conductivity by approximately 24%. For material 5, the variation of the material's conductivity is close to the experimental uncertainty in the nonlaminated materials. Conversely, for material 6 (Fig. 10b), the conductivity predicted using the total model overestimates conductivity by approximately 27%, and the average normalized conductivity of the fiber only model (0.036) is quite close to that of the real material (0.034). The variation in experimental conductivities measured (Fig. 10b) was larger than the experimental uncertainty. Intrinsic material variation may have been exacerbated by breaking of fibers internal to the electrode during the lamination process; SEM images of laminated and nonlaminate samples did not show any significant difference on the surface lay-

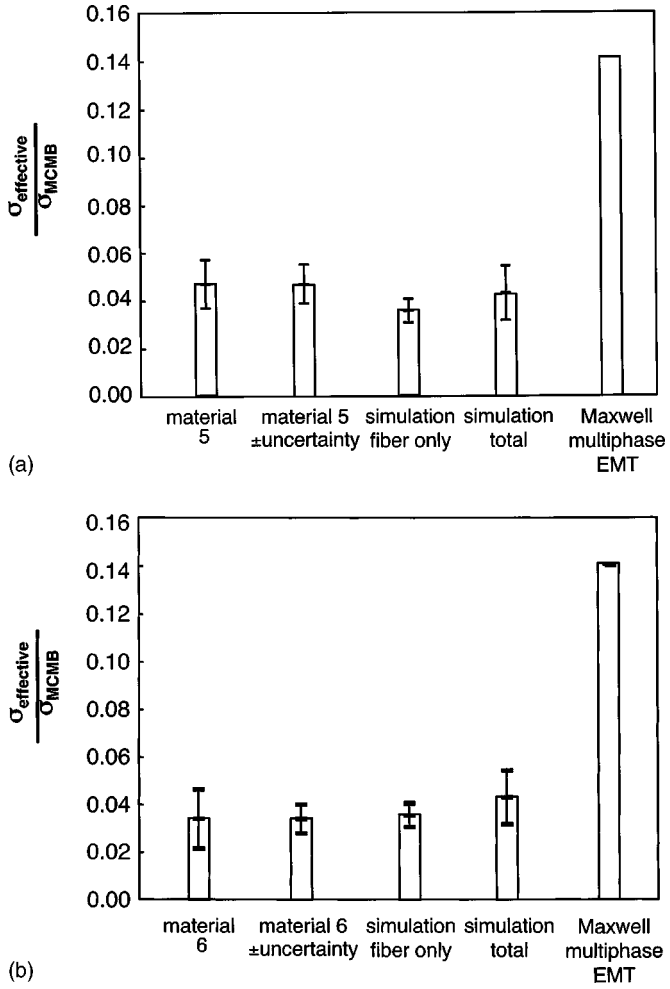

Figure 10. Simulation and experimental results for IREQ fibrous nonlaminated (material 5) and laminated (material 6) materials are shown in (a) and (b), respectively. Simulation models assumed normally distributed fibers of average aspect ratio 6.8 ± 6.8, based on image analysis. The Maxwell multiphase effective medium theory is given for reference.

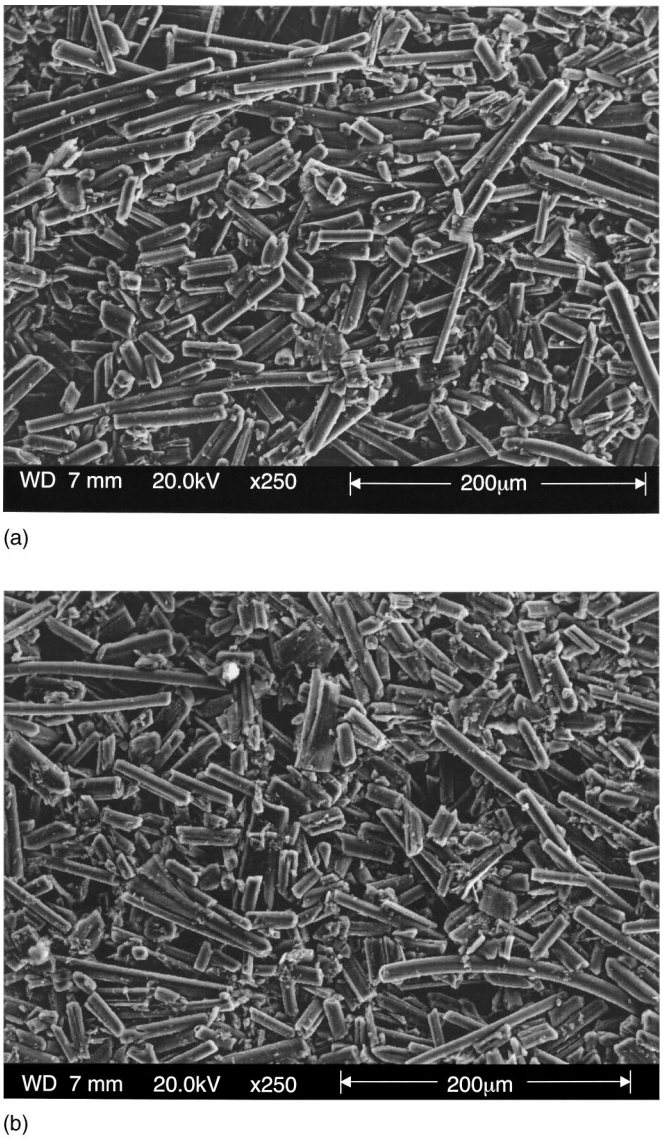

Figure 11. Scanning electron micrographs of (a) material 5 and (b) material 6, showing fibers to have very smooth surfaces.

ers. The conductivities of laminated sample are, however, smaller than those of the nonlaminated samples, implying higher internal resistance. Further investigation will be needed in order to identify the cause of the differences between laminated and nonlaminated material conductivity.

Discussion

Clearly, effective medium theories, even with multiphase assumptions, do not provide sufficiently accurate predictions of electrode transport properties to allow better design. Our previous work had shown that even rigorous bounds on behavior of microstructure cannot narrow predictions of material properties, especially in high contrast materials, since the continuity assumption, (the major assumption of variational methods), is violated.

Comparison of materials studied.—Results in Table III show that contact resistivity of laminated materials is lower than that of nonlaminated materials except for materials 5 and 6, which may be due to better particle connection. Also, contact resistances of materials 1 and 2 were determined to be about ten times larger than those of the other materials studied. This may be because natural graphite flakes have larger contact areas than spherical and cylindrical particles. Additionally, delamination and cracks on the active material layer may result in poor connection between active material and copper foil. Contact resistivities of materials 3 and 4 were smaller than those of materials 5 and 6, possibly due to differences in the contact areas of MCMB spheres and the carbon fiber cylinders. As mentioned previously, the particle shape has a profound effect on the contact resistance between the active materials and the copper foil. Active material contact resistance was lowest for MCMB (spherical), and highest for natural graphite (flake), with intermediate values for fibers (cylinders).

Since material 1 did not contain conductive particles at sufficiently high volume fraction, simulated domains were not percolated, and the numerical approach failed to give reasonable predictions. This is generally true of the computational approach at present: for regions of high phase contrast but unpercolated conductive phases, the numerical approach cannot be used effectively. However, materials of present interest for use as conductive additives generally contain sufficient volumes of particles for percolation, in order to obtain reasonably high conductivities. Thus, the application of the simulations to these materials is appropriate for determining the shapes and fractions of the various conductive particles used, rather than the effects of very small overall volumes of conductive materials.

It is well known that percolation threshold depends strongly on the particle shape; Pike and Seager[24] found the percolation threshold

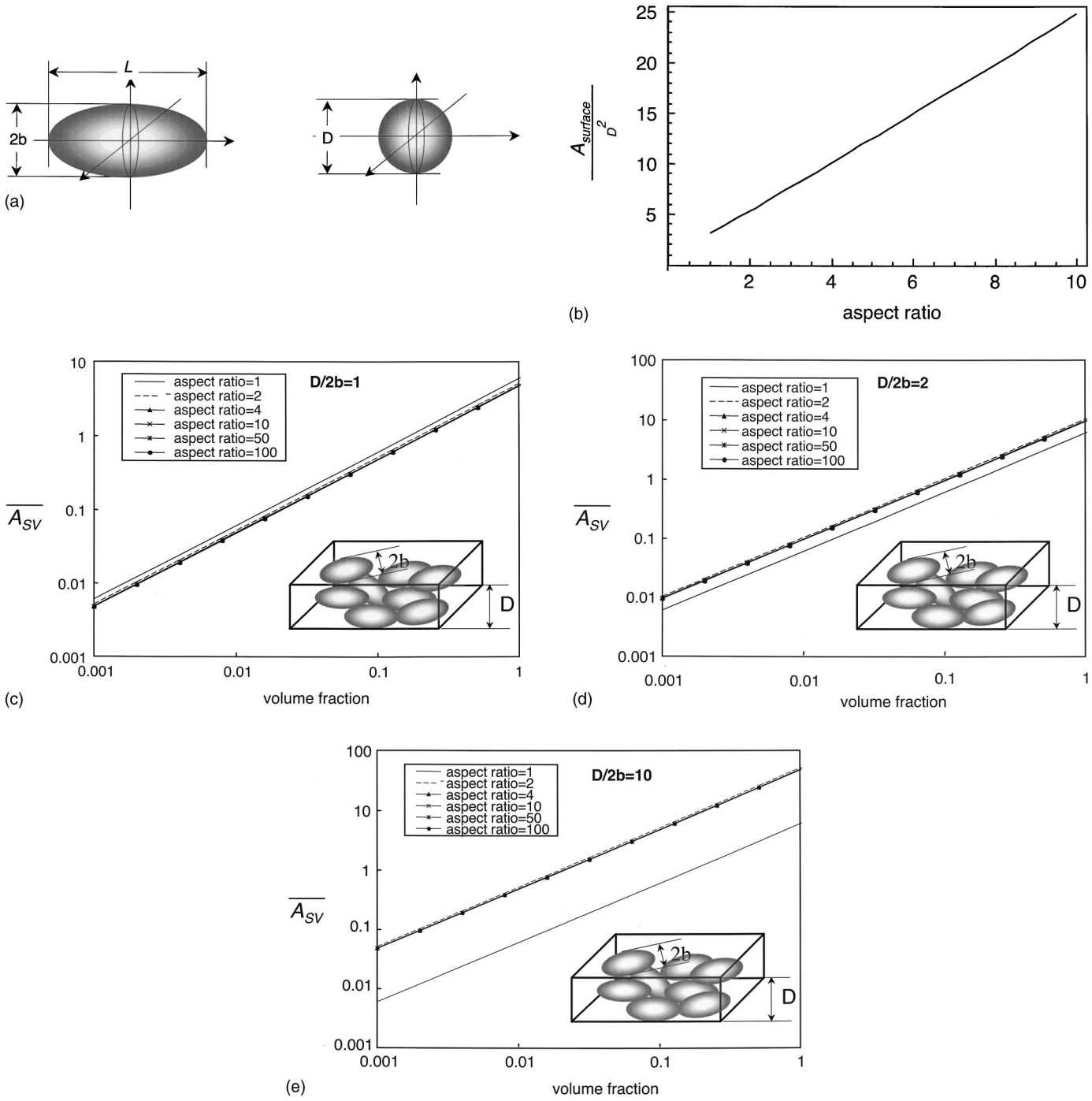

Figure 12. (a) Schematic representation of ellipsoid and spherical particles with dimensions, and (b) resulting normalized surface area *vs.* AR (b). $\overline{A}_{SV}$ *vs.* volume fraction are also shown for (c) $D/2b = 1$, (d) $D/2b = 2$, and (e) $D/2b = 10$.

for uniform spheres to be about 30%. Our previous work showed that increasing the particle AR by a small amount lowers the percolation threshold dramatically, simultaneously decreasing variability in resistivity. Comparison of the error bars of Fig. 8-10 illustrates the trend of increased variability with decreased AR.

Two manufacturing processes, laminated and nonlaminated, were also examined here. The conductivities of the laminated anodes, with the exception of material 6, were larger than those of the nonlaminated anodes. Conversely, the variation of conductivity and the contact resistances between the carbon and copper layers of the laminated anodes were smaller than those of the nonlaminated anodes with the exception of material 5 and 6. These results indicate better interparticle connections and connections between particles and current collectors in the laminated materials. In material 6, however, variation of material conductivity was larger than the experimental uncertainty.

Model application: importance of surface area.—The surface area of the anode is a crucial physical property; it has been hypothesized that a relationship between the surface area of the anode and the irreversible capacity loss (ICL) of the anode may be established.[49] In order to allow use of these conduction models for

various shapes of particles, we provide a few simple geometrical relations for calculation of total surface area for various morphologies of electrode materials. Assuming that the substrate is comprised of particles having the same AR, x, denoted as $x = L/2b$, the particle volume for both ellipsoid and spherical shapes shown in Fig. 12a, may be expressed as

$$V_{\text{particle}} = \begin{cases} \dfrac{\pi L(2b)^2}{6} = \dfrac{\pi x(2b)^3}{6} & \text{for elliptical particle} \\ \dfrac{\pi D^3}{6} & \text{for spheres} \end{cases} \quad [19]$$

where D is the sphere's diameter, L is the two times the major axis length, and b is the minor axis length. The surface area of an individual particle may be defined as

$$A_{\text{particle}} = 2\pi\left[\frac{(2b)^2}{4} + \frac{L^2(2b)}{4\sqrt{L^2-(2b)^2}}\sin^{-1}\left(\sqrt{1-\left(\frac{2b}{L}\right)^2}\right)\right]$$
$$= 2\pi\left[\frac{(2b)^2}{4} + \frac{x^2(2b)^2}{4\sqrt{x^2-1}}\sin^{-1}\left(\sqrt{1-\left(\frac{1}{x}\right)^2}\right)\right] \quad [20]$$

If $x \to 1$ (*i.e.*, a spherical particle), then A_{particle} is as $2b = D$

$$A_{\text{particle}} = D^2\pi \quad [21]$$

The relationship between surface area and AR is shown for reference in Fig. 12b, wherein the well-known minimum of surface area occurs for spheres when the length of the ellipsoid minor axis equals the radius of the sphere. The family of curves seen in Fig. 12c-e, illustrate the relationships among particle size, particle surface area, AR, and volume fraction. In each plot, the ratio $D/2b$ is varied, where D is the height of the rectangular domain of interest and also the constrained diameter of the sphere (*i.e.*, no stacked spheres in the vertical direction), and $2b$ is the length of the minor axis of the particle which can be varied. We use the dimensionless value $\overline{A}_{\text{SV}}$ to relate the particle surface area, the height of the rectangular box, and the spherical diameters of the particles as

$$\overline{A}_{\text{SV}} = \frac{A_{\text{surface}}D}{V_{\text{region}}} \quad [22]$$

where A_{surface} is the summation of all particles' area, and V_{region} is the volume of the interest in the rectangular domain. In Fig. 12c-e, $\overline{A}_{\text{SV}}$ is plotted *vs.* volume fraction. Fig. 12c shows that for specific cases of particle diameter ($D = 2b$) for any volume fraction and rectangular box volume, the smaller the AR, the more particles can be packed into the rectangular region. In Fig. 12d and e, the opposite trend is seen; when $2b$ is smaller than D, (*i.e.*, larger AR > 1), more particles may be packed in the rectangular box. Consequently, additional surface area is gained.

Thus, for smaller minor axis length (b), more particles can be packed inside a rectangular domain. For materials of interest here, the particle minor axis length is smaller for larger aspect ratio particles than for smaller aspect ratio particles. For example, in the IREQ materials studied, the MCMB aspect ratios were 1, with diam of 22 μm, and the fiber ARs were 6.8, with diam of 10 μm. Therefore, the surface area of an anode containing only fibers may be significantly larger than an anode containing only MCMB particles, even though the volume fractions are the same.

Our own previous experimental work on NiMH battery cathode conductivity has shown that moderate increases in particle ARs provide significant conductive benefits[50] since larger particle/fiber ARs render significantly diminished percolation points. However, use of higher AR materials significantly affects overall, normalized surface area available for reaction.

Conclusions and Future Work

The results of this study may offer some insight into the design and selection of active materials. Selection of appropriate blends of conductive additives is presently a problem of high interest to manufacturers, and the results presented here show that such selection can be made through use of modeling. The models presented were shown to have applicability to a wide variety of materials, including those comprised of fibers, particles, and flakes. Validation of the models was made in several types of materials, containing all of these geometries of conductive additives.

The four-point-probe technique proved applicable to the electrode materials tested. Extension of the Schumann-Gardner multilayer theory resulted in a method for determining the effective conductivity of the active materials and the contact resistance between the active materials and the current collectors. This work allowed validation of the numerical approach in simulating conduction in multiphase arrays as applied to battery electrodes.

The variation in conductivity of the various graphitized carbon materials was clearly shown to be related to the morphology of the active materials. The natural graphite has previously been shown to have the highest capacity with long voltage plateau during charging and discharging.[51] However, because of its flaked shape, having higher contact area, the contact resistance between the active material and current collector may be significant. Natural graphite may, in fact, be inherently unsuitable for some fast charge/discharge applications. On the other hand, MCMBs and graphitized carbon fibers show lower capacity,[3-5,8-15] but because of their low resistivities and special geometries, effective resistivity and contact resistance may possibly be minimized for the electrode. Ultimately, the trade-offs among factors in electrochemical performance can be resolved with improved simulations of materials performance. An obvious subject of future work is combined electrochemical, conduction, and mechanical modeling of these materials. Further work on interaction between particles and the current collector is also probably warranted.

Acknowledgments

This work was generously supported by the Department of Energy BATT Program, and the Synthetic Multifunctional Materials Program of DARPA (Dr. Leo Christodoulou, Program Director, DARPA; Dr. Steve Fishman, Program Director, ONR). Additional support was provided by the University of Michigan WIMS-ERC (Cook), and an NSF PECASE Award (Sastry). Materials and technical advice were provided by LBNL (Dr. Kim Kinoshita, Dr. Frank McClarnon), Argonne National Laboratory (Dr. Gary Henriksen), and IREQ (Dr. Karim Zaghib). These sponsors and colleagues are gratefully acknowledged.

One of the authors, A. M. Sastry, assisted in meeting the publication costs of this article.

List of Symbols

	variable
$\overline{A}_{\text{SV}}$	normalized particle total surface area with V_{region} multiply by D
A	anode
a	probe radius
A_{particle}	particle surface area
b	length of minor axis
C	cathode
D	diameter (sphere)
d	copper foil thickness
d_{002}	distance between basal planes
f	volume fraction
I	current
J_0	zero order of the first kind of Bessel function
K_m	effective conductivity
L	particle length
P	power
p	probability
p_c	critical probability threshold
R_b	internal resistance
R_c	resistance between current collectors and electrode
R_e	electrode resistance

R_{in}	interface resistance
R_s	electrolyte resistance
S	probe spacing
V	voltage
V_n	voltage function of nth layer
V_{oc}	open-circuit voltage
$V_{particle}$	particle volume
V_{region}	volume of interest region
w_i	uncertainty of i variable
x	aspect ratio
ΔV_n	voltage function between the second and the third probes of nth layer

Greek

θ_n, ψ_n	Kernel functions
ρ_1	resistivity of carbon compound
ρ_2	effective resistivity of copper foil and contact resistivity
ρ_c	contact resistance
σ	conductivity

References

1. J. B. Goodenough, in *Lithium Ion Batteries, Fundamentals and Performance*, M. Wakihara and O. Yamamoto, Editors, p. 1, Wiley-VCH Verlag GmbH, Weinheim, Germany (1998).
2. A. Herold, *Bull. Soc. Chim. Fr.*, **7-8**, 999 (1955).
3. A. Mabuchi, K. Tokumitsu, H. Fujimoto, and T. Kasuch, *J. Electrochem. Soc.*, **142**, 1041 (1995).
4. A. Mabuchi, H. Fujimoto, K. Tokumitsu, and T. Kasuh, *J. Electrochem. Soc.*, **142**, 3049 (1995).
5. C. H. Doh, S. I. Moon, M. S. Yun, and D. H. Yum, *Bull. Korean Chem. Soc.*, **21**, 169 (2000).
6. E. Buiel and J. R. Dahn, *Electrochim. Acta*, **45**, 121 (1999).
7. T. Numata, C. Amemiya, J. Iriyama, T. Miura, and M. Shirakata, *NEC Res. Dev.*, **41**, 8 (2000).
8. S. Ahn, *Electrochem. Solid-State Lett.*, **1**, 111 (1998).
9. N. Takami, A. Satoh, M. Hara, and T. Ohsaki, *J. Electrochem. Soc.*, **142**, 2564 (1995).
10. T. Ohsaki, M. Kanda, Y. Aoki, H. Shiroki, and S. Suzuki, *J. Power Sources*, **68**, 102 (1997).
11. M. Endo, C. Kim, T. Karaki, T. Kasai, M. J. Matthews, S. D. M. Brown, M. S. Dresselhaus, T. Tamaki, and T. Nishimura, *Carbon*, **36**, 1633 (1998).
12. M. Endo, J. I. Nakamura, A. Emori, Y. Sasabe, K. Takeuchi, and M. Inagaki, *Mol. Cryst. Liq. Cryst.*, **245**, 171 (1994).
13. K. Tatsumi, K. Zaghib, Y. Sawada, H. Abe, and T. Ohsaki, *J. Electrochem. Soc.*, **142**, 1090 (1995).
14. K. Suzuki, T. Iijima, and M. Wakihara, *Electrochim. Acta*, **44**, 2185 (1999).
15. H. Abe, T. Murai, and K. Zaghib, *J. Power Sources*, **77**, 110 (1999).
16. G. Henriksen, Private communication Argonne National Laboratories (2001).
17. J. C. Maxwell-Garnett, *Philos. Trans. R. Soc. London, Ser. A*, **204**, 385 (1904).
18. D. A. G. Bruggeman, *Ann. Phys. (Leipzig)*, **24**, 636 (1935).
19. R. E. Meredith and C. W. Tobias, in *Advances in Electrochemistry and Electrochemical Engineering*, C. W. Tobias, Editor, p. 15 Wiley Interscience, New York (1962).
20. D. Stroud, *Phys. Rev. B*, **12**, 3368 (1975).
21. T. C. Choy, *Effective Medium Theory: Principles and Applications*, p. 19, Oxford University Press, New York (1999).
22. Z. Hashin and S. Shtrikman, *J. Appl. Phys.*, **33**, 3125 (1962).
23. S. Kirkpatrick, *Rev. Mod. Phys.*, **45**, 574 (1973).
24. G. E. Pike and C. H. Seager, *Phys. Rev. B*, **10**, 1421 (1974).
25. X. Cheng, A. M. Sastry, and B. E. Layton, *ASME J. Eng. Mater. Technol.*, **123**, 12 (2001).
26. X. Cheng and A. M. Sastry, *Mech. Mater.*, **31**, 765 (1999).
27. Y.-B. Yi and A. M. Sastry, *Phys. Rev. E*, (2002); Submitted.
28. Y.-B. Yi and A. M. Sastry, *Proc. R. Soc. London, Ser. A*, (2002); Submitted.
29. C. W. Wang, L. Berhan, and A. M. Sastry, *ASME J. Eng. Mater. Technol.*, **122**, 450 (2000).
30. C. W. Wang and A. M. Sastry, *ASME J. Eng. Mater. Technol.*, **122**, 460 (2000).
31. A. M. Sastry, in *Comprehensive Composite Materials*, C. H. Zweben and A. Kelly, Editors, p. 609, Elsevier, New York (2001).
32. A. M. Sastry, X. Cheng, and C. W. Wang, *Journal of Thermoplastic Composite Materials*, **11**, 288 (1998).
33. D. H. Dickey, in National Bureau Standards *Spreading Resistance Symposium Proceedings*, NBS, Special Publication, 400-10, p. 45-50 (1974).
34. J. Albers and H. L. Berkowitz, *J. Electrochem. Soc.*, **131**, 392 (1984).
35. D. K. Schroder, *Semiconductor Material and Device Characterization*, 2nd ed., p. 1, John Wiley & Sons, New York (1998).
36. L. B. Valdes, *Proc. of the Institute of Radio Engineers*, **42**, 420 (1954).
37. P. A. Schumann and E. E. Gardner, *J. Electrochem. Soc.*, **116**, 87 (1969).
38. J. J. Kopanski, J. Albers, G. P. Carver, and J. R. Ehrstein, *J. Electrochem. Soc.*, **137**, 3935 (1990).
39. S. C. Choo, M. S. Leong, and K. L. Kuan, *Solid-State Electron.*, **19**, 561 (1976).
40. H. L. Berkowitz and R. A. Lux, *J. Electrochem. Soc.*, **126**, 1479 (1979).
41. http://www.matweb.com.
42. S. C. Choo, M. S. Leong, H. L. Hong, L. Li, and L. S. Tan, *Solid-State Electron.*, **21**, 769 (1978).
43. S. C. Choo, M. S. Leong, and L. S. Tan, *Solid-State Electron.*, **24**, 557 (1981).
44. J. P. Holman, *Experimental Methods for Engineers, 4th ed.*, p. 50, McGraw Hill, New York (1984).
45. W. Primak and L. H. Fuchs, *Phys. Rev.*, **95**, 22 (1954).
46. *MCMB Resistivity Data*, Osaka Gas Co. Ltd, R&D Center, Osaka, Japan, http://www.c-direct.ne.jp/osaka/english.
47. *PVdF Resistivity Data*, Quadrant Engineering Plastic Products, http://www.matweb.com.
48. http://rsb.info.nih.gov/nih-image/
49. K. Zaghib, F. Brochu, A. Guerfi, and K. Kinoshita, *J. Power Sources*, **103**, 140 (2001).
50. C. W. Wang, X. Cheng, A. M. Sastry, and S. B. Choi, *ASME J. Eng. Mater. Technol.*, **121**, 503 (1999).
51. M. Fujimoto, Y. Shoji, Y. Kida, R. Ohshita, T. Nohma, and K. Nishio, *J. Power Sources*, **72**, 226 (1998).